Microlens arrays with adjustable aspect ratio fabricated by electrowetting and their application to correlated color temperature tunable light-emitting diodes

JUNCHI CHEN,[1,4] BENJAMIN FRITZ,[2,4] GUANWEI LIANG,[1] XINRUI DING,[1,*] ULI LEMMER,[2,3] AND GUILLAUME GOMARD[2,3,5]

[1]*South China University of Technology, China*
[2]*Light Technology Institute (LTI), Karlsruhe Institute of Technology (KIT), Engesserstrasse 13, 76131 Karlsruhe, Germany*
[3]*Institute of Microstructure Technology (IMT), Karlsruhe Institute of Technology (KIT), Hermann-von-Helmholtz-Platz 1, 76344 Eggenstein-Leopoldshafen, Germany*
[4]*These authors contributed equally*
[5]*guillaume.gomard@kit.edu*
[*]*dingxr@scut.edu.cn*

Abstract: We develop a facile, fast, and cost-effective method based on the electrowetting effect to fabricate concave microlens arrays (MLA) with a tunable height-to-radius ratio, namely aspect ratio (AR). The electric parameters including voltage and frequency are demonstrated to play an important role in the MLA forming process. With the optimized frequency of 5 Hz, the AR of MLA are tuned from 0.057 to 0.693 for an increasing voltage from 0 V to 180 V. The optical properties of the MLA, including their transmittance and light diffusion capability, are investigated by spectroscopic measurements and ray-tracing simulations. We show that the overall transmittance can be maintained above around 90% over the whole visible range, and that an AR exceeding 0.366 is required to sufficiently broaden the transmitted light angular distribution. These properties enable to apply the developed MLA films to correlated-color-temperature (CCT)-tunable light-emitting-diodes (LEDs) to enhance their angular color uniformity (ACU). Our results show that the ACU of CCT-tunable LEDs is significantly improved while preserving almost the same lumen output, and that the MLA with the highest AR exhibits the best ACU performance.

1. Introduction

Microlens arrays (MLA) are micro-optical elements widely used in optical sensors [1], photovoltaics [2], 3D displays [3] as well as for light management in light emitting diodes (LEDs) [4,5]. The LED technology offers unique advantages compared to traditional incandescent bulbs and fluorescent lamps including a high efficiency, a low power consumption and a long lifetime [6–9]. To meet the demands of high-quality illumination and display, the angular color uniformity (ACU) of LEDs needs further improvement [10–12]. Numerous methods have been proposed to ameliorate the ACU of white LEDs, such as light scattering nano-particles [13,14], shaped phosphor layers [15,16], diffusing reflectors [17] and microstructured films [18,19]. Among these different approaches, the microstructured films method is particularly attractive as it is facile and suitable for various LED packages, and has been widely adopted in commercial applications. Furthermore, Chen et al. demonstrated that diffusing MLA significantly improve the ACU of correlated color temperature (CCT)-tunable LEDs [20], which motivated the present work. As a new type of intelligent LED light source, a CCT-tunable LED changes the CCT by independently adjusting the light intensity of cold and warm color light [21,22]. Because of the lack of a

proper light mixing scheme, CCT-tunable LED lamps suffer from a poor color uniformity and from the appearance of a blue circle and a yellow halo, which are detrimental to the illumination quality [23]. In our previous research, we effectively improved the ACU of CCT-tunable LEDs by MLA, reducing the CCT deviation from 1090 K to 218 K within the CCT range of 3000-4000 K [20]. Herein, the MLA morphology and more specifically their aspect ratio (AR), defined as the ratio of their height over their base radius, is a key factor for the ACU performance, which still needs to be investigated.

The increasing demand for micro-optoelectronic devices has prompted the development of MLA fabrication methods including direct laser writing [24–26], reactive ion etching [27,28], cylindrical micropillars photoresist reflow [29–31], hot embossing [32–34] and inkjet printing [35,36]. Direct laser writing enables fabrication of MLA with different shapes. However, it is not suitable for mass fabrication because it is a serial process. Reactive ion etching requires vacuum which is slowing down fabrication. Photoresist reflow and hot embossing methods have the advantages of low cost and high surface flatness, but the lens morphology is hard to control. Many studies have shown that the microlenses shape has a significant impact on the MLA performance [37–39], hence the fabrication of morphology-controllable MLA has attracted much attention. Xu et al. controlled the curvature of the acrylate resin concave meniscus in a patterned PDMS template. To this end, the interfacial energy was adjusted by the processing time for the surface modification of the PDMS microholes [40]. Fang et al. used the UV laser writing method coupled with soft imprint technology to fabricate paraboloidal MLA with varying ARs, which can be easily tuned by changing the exposure laser power [41]. A breath figure method based on water fog condensing was proposed by Peng et al. to fabricate the MLA by adjusting the condensing temperature and time [42]. Yang et al. proposed to fabrication hexagonal compound eye MLA using a maskless lithography technique based on digital micromirror device which allowed a proper control of the morphology. To achieve this, three steps were involved and a final reflow process was required to smoothen the lenses' surface [43]. The above described methods can form MLA structures with varying ARs, but they do not allow to rapidly change them during fabrication.

In our study, we propose to exploit a versatile, potentially low-cost and rapid route based on the electrowetting effect in order to fabricate concave MLA with controllable lens curvature [44,45]. The electrowetting phenomenon refers to the change in solid-liquid contact angle due to an applied potential difference between the solid and the liquid [46]. In our approach, liquid UV-cured polymer is filling the micro-holes of a patterned silicon template, whose preparation only requires one initial wet etching step and determines the diameter and arrangement of the MLA. Their AR can then be controlled by adjusting the voltage and frequency between the silicon template and the polymer which changes the contact angle of the polymer surface. In this contribution, we specifically tune these electrical parameters with a view to maximizing the AR of the MLA. Our objective is here to broaden the transmitted light angular distribution, to promote light mixing and in turn, to improve the ACU of CCT-tunable LED lamps. This demonstration is supported in the next sections by both spectroscopic measurements and (ray tracing) optical simulations, and by testing the developed MLA in CCT-tunable LED lamps.

2. Experimental and simulation methods

2.1 Fabrication of MLA with tunable AR by electrowetting

The concave MLA fabrication method we use requires a micro-patterned template and the application of an electrical field, as schematized in Fig. 1. First, UV curable polymer (Norland optical adhesive 65) was spin-coated on a glass substrate covered by a transparent conductive indium tin oxide (ITO) layer (Shenzhen Xiangcheng). A P-type doped conductive silicon template (with electrical resistance between 1 and 10Ω/cm), drilled by a hexagonal array of cylindrical micro-holes, was placed on the polymer layer while sufficient pressure was applied to confine the polymer in the holes, as shown in Fig. 1(a). In this study, the

micro-hole array was fabricated by conventional photolithography and wet etching. The diameter and arrangement of the MLA are determined by the design of the micro-holes array in the template. Their AR can be precisely controlled by the electric field. In order to provide enough space for the deformation of liquid polymer, the micro-holes depth should be much larger than the thickness of the polymer layer and was therefore set to 50 μm. A 600 nm thick dielectric silicon dioxide layer was subsequently formed on the template surface by thermal oxidation so as to enhance the electric field strength [47–49]. Before the electrowetting process, fluoroalkyl silane alcohol solution (Trichloro(1H,1H,2H,2H-perfluorooctyl) silane) was spin coated on the surface of the template and dried as an anti-adhesion layer. Then voltage was applied between the template and the conductive substrate to create an electric field that changes the curvature of the meniscus polymer surface in the hole array, as shown in Fig. 1(b). The voltage was driven by a waveform generator (Agilent 33250A) and a high voltage power supply (Trek Model 610E). While pressure and voltage were maintained, UV light was irradiated from the ITO coated glass substrate side to cure the polymer, as shown in Fig. 1(c). Finally, the conductive silicon template was separated from the ITO glass substrate and concave MLA films were obtained, as shown in Fig. 1(d). In order to generate replicas after the fabrication of the MLA film, polydimethylsiloxane (PDMS, Dow Corning 184) was spin-coated on the MLA film and separated after curing as a negative imprint template. By using the PDMS negative mold to soft imprint a UV curable polymer layer (Norland optical adhesive 65), multiple copies of the MLA film were reobtained facilely. In this method, the structured silicon template can be re-used to fabricate MLA with different ARs by simply changing the conditions of the applied electrical field, thereby limiting the cost of the process.
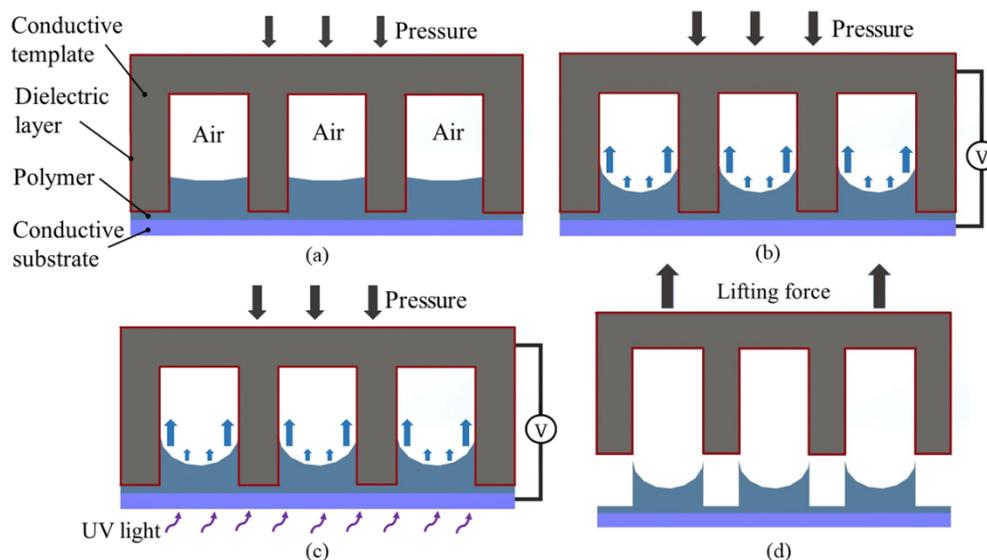
Fig. 1. Schematic illustration of concave MLA fabrication by the electrowetting process. (a) Coating of a polymer layer on the bottom transparent conductive oxide substrate and contact of the micro-patterned template onto the polymer layer with a certain pressure to confine the polymer in the micro-holes; (b) Application of a voltage between the template and the conductive substrate under controlled pressure; (c) UV irradiation from the transparent conductive oxide substrate side to cure the polymer; (d) Separation of the template from the cured polymer.

2.2 Simulation methodology

2.2.1 Electrowetting simulations

The fabrication process was simulated using the finite element method (FEM) implemented in a commercial software (COMSOL Multiphysics version 5.3).

For that purpose, we used a fluid mechanics model and an electric field model to describe the fluid motion during the electrowetting process. According to the electro-hydrodynamics principle, the movement of a fluid in an electric field can be described by the Navier−Stokes equation of momentum and mass conservation [50]:

$$\begin{cases} \rho\dfrac{\partial \vec{u}}{\partial t} + \rho\vec{u}\cdot\nabla\vec{u} = -\nabla p + h\nabla^2\vec{u} + \dfrac{1}{3}h\nabla\left(\nabla\cdot\vec{u}\right) + f^e + \rho g \\ \dfrac{\partial \rho}{\partial t} + \nabla\left(\rho\vec{u}\right) = 0 \end{cases}, \tag{1}$$

where ρ and η denote the fluid's mass density and viscosity, respectively, p is the hydraulic pressure in the fluid, f^e denotes the volumetric force generated by an electric field, $\vec{u}$ is the fluid flow rate, g is gravitational acceleration and t represents time. The equation of motion sets the fluid flow in the model as non-compressible with momentum conservation. According to Maxwell's equation, the volumetric force f^e has mainly three manifestations: Coulomb force, electrostrictive force, and dielectrophoresis (DEP) force. DEP force is the force which is exerted on a dielectric material when it is subjected to a non-uniform electric field. Because the fluid used in this study is a dielectric polymer that has no free charge and the electric field strength is insufficient to generate noticeable electrostrictive forces, the electric volumetric force formula can be simplified to:

$$f^e = -\frac{1}{2}E^2\nabla\varepsilon \tag{2}$$

where E represents the electric field intensity and ε represents the fluid's dielectric constant. In an electric field, the liquid molecules experience electric polarization. In a uniform electric field, polarization molecules are evenly distributed and offset each other without showing DEP force. In a non-uniform electric field, the distribution of polarization molecules is directional. The DEP forces of molecules cannot offset each other and always point in the direction of the stronger electric field region. In addition, the representation of the liquid interface layer was described by a troposphere in this study, and is described by the basic phase function φ [51,52]. According to Eq. (2), the electric volumetric force f^e is only concentrated at the gas-liquid interface as the gradient of the dielectric constant ε of the polymer-air system varies greatly in this region.

In our simulation model, the thickness of the dielectric layer was set to 0.6 µm, as measured experimentally, and the minimum distance between the template and the substrate to 2 µm. Lastly, the polymer volume was fixed. The DEP force distribution and the motion of the polymer were simulated under varying voltages of 60 V, 120 V and 180 V.

2.2.2 Ray tracing simulations

Light transmission through the MLA films was simulated using the commercial software LightTools (Synopsys). The schematic diagram of the optical simulations is shown in Fig. 2(a). In our model, 10^8 parallel rays are incident on the patterned side of the MLA films and one-period unit is illuminated, as depicted in the close-up shown in Fig. 2(b). The actual 3D morphology of the MLA film is extracted from laser scanning confocal microscope to establish a realistic model based on concave micro-lenses with a diameter of 20 µm and on a

hexagonal array with a pitch of 30 μm. The hemispherical detector surrounds the film and the light intensity distribution is obtained. Owing to the symmetric distribution of the MLA, the simplification does not affect the simulation accuracy. The refractive index of the MLA film is set to 1.524, which corresponds to the refractive index value of NOA65.
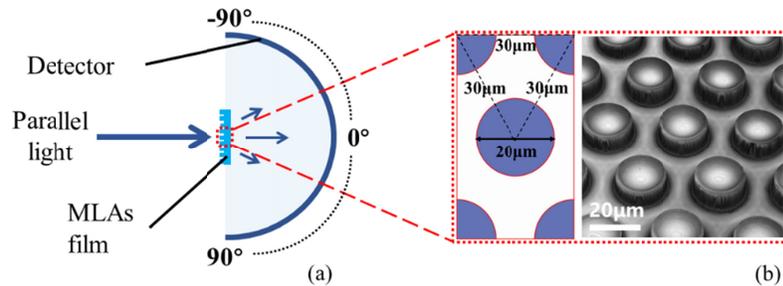
Fig. 2. (a) Schematic illustration of the ray-optics simulations framework. Parallel light is incident to the patterned side of the MLA films, and the transmitted light is captured by a hemispherical detector. (b) Simulated unit cell of the concave MLA with hexagonal arrangement (left), and corresponding scanning electron microscope image of the fabricated MLA at a tilt angle of 45°(right).

2.3 Characterizations

The MLA films fabricated in this study were applied to a CCT-tunable LED lamp for optical measurement. The structure of the CCT-tunable LED used in this study is shown in Fig. 3(a). The size of the plate is 18 mm x 24 mm. The LED system consists of a ring-shaped (4.3 mm inner radius, 7.5 mm outer radius) cool-white area and a circular (R = 3.9 mm) warm-white area inside the ring. The cool-white area is made up of blue light LED chips encapsulated by 7.85 wt% yellow YAG phosphor with the peak emitting wavelength of 533 nm and 0.65% wt% red YAG phosphor with peak emitting wavelength of 625 nm and has a CCT between 6200 and 6500 K. The warm-white area is encapsulated with 10.96 wt% yellow YAG phosphor with peak emitting wavelength of 533 nm and 2.35% red YAG phosphor with peak emitting wavelength of 630 nm, and its CCT is between 2500 and 2800 K. The LED chips of these two areas are driven separately and the CCT can be controlled conveniently from 2500 K to 6500 K by adjusting the ratio of the driven currents of the two areas. The CCT-tunable LED is mounted on an aluminum fin to reduce the effect of LED junction temperature on the measurement, as shown in Fig. 3(b). The schematic diagram of the CCT-tunable LED lamp packaged with MLA film is shown in Fig. 3(c).
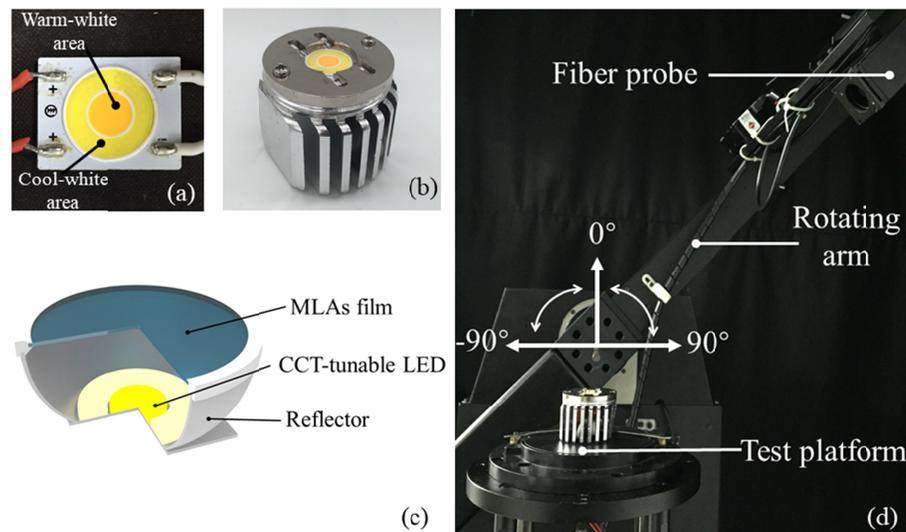
Fig. 3. (a) Photograph of CCT-tunable chip on board LED. (b) CCT-tunable LED mounted with aluminum fins. (c) Schematic diagram of CCT-tunable LED lamp packaged with MLA film. (d) Image of home-made CCT distribution measurement system.

A laser scanning confocal microscope (Olympus LEXT OLS4000) was used to measure the geometries of the MLA surface formed using different electrical parameters. An ultraviolet-visible spectrometer (Beijing Puxi, TU-1901) was used to characterize the overall (specular and diffuse) transmittance and the haze (fraction of diffused transmitted light to the overall transmitted light) of the MLA films. Light was incident on the MLA side at normal direction and the spectra were acquired from 450 nm to 780 nm. In the ACU measurement, a home-made test system was used to obtain the CCT distribution, as shown in Fig. 3(d). The luminous flux values at different CCT ranges, powered by a Keithley 2450 DC source, were measured by a 0.5 m integrating sphere coupled to a spectrometer (Otsuka LE5400)

3. Results and discussion

To explore the influence of the electrical parameters on the microlenses profile, we fabricated MLA films under different voltages and frequencies. The influence of the applied voltage on the MLA morphology was first investigated. Figure 4(a) shows the MLA film surface contours under different constant voltage, resulting in AR values of 0.057 (0V), 0.300 (60V), 0.366 (120V) and 0.373 (180V). In the absence of applied voltage, the surface contour of the MLA is nearly flat. Under applied voltage, the contour curvature of the MLA surface increases and starts saturating at 180 V. This saturation is caused by the charges trapped by the dielectric layer. The electrical polarization charges in the liquid will enrich at the liquid-solid interface under an external electric field. When the voltage is too high, the charges in the liquid will start to cross the interface and enter the conductive template like a slight dielectric breakdown, which weakens the electric potential of the interface [53]. Therefore, the contour curvature of MLA does not evolve anymore above 180 V and the maximum AR value that is achieved is 0.373.

To further increase the saturation value of the applied voltage, square wave voltages at different frequencies were applied during the fabrication process as shown in Fig. 4(b). The corresponding AR obtained are 0.366 (0Hz), 0.503 (1Hz), 0.547 (5Hz), 0.603 (25Hz) and 0.263 (125Hz). Compared with constant voltages, square wave voltages between 1 and 25 Hz produce a larger sag height. Indeed, when the external voltage exceeds the saturation value, the charge enters the dielectric layer, forming a reverse electric field. Because there is a certain hysteresis in the charge migration, when the applied voltage reverses, the electrons

need time to migrate in reverse. Before the charges finish migrating, the reverse electric field and the external electric field form a short-term codirectional superposition, making the electric field stronger than in the saturated state [53]. Under a certain frequency of reversing, the superposition electric field can maintain a stable value that is higher than the pristine saturation voltage, so the contour curvature formed under the square wave voltage condition is larger.

Owing to the better smoothness and sag height of the MLA produced, 5 Hz was selected as the frequency for the next tests. Figure 4(c) shows the contour comparison of the MLA formed under different 5 Hz square wave voltages. The resulting AR value are 0.057 (0V), 0.212 (60V), 0.547 (120V) and 0.693 (180V). As previously described, the surface curvature gradually increases with increasing voltage amplitude and reaches a maximum AR of 0.693. Compared with the constant voltage of the same magnitude, square wave voltage provides higher saturation voltages and achieves higher sag heights. By regulating the square wave voltage amplitude, the AR of the MLA can be tuned over a broad range. In the following, we refer to the planar polymer film as the "Smooth Film", and to the concave MLA films formed by a square wave voltage of 0 V, 60 V, 120 V and 180 V as "S-0 film", "S-60 film", "S-120 film", and "S-180 film", respectively. The macroscopic and microscopic images of S-0 film and S-180 film are shown in Fig. 4(d). It can be clearly seen that the AR of the S-180 film is significantly larger than S-0 film and the MLA has good spatial homogeneity.

Details on the DEP force distribution and the morphology variation obtained from FEM simulations are shown in Fig. 4(e). The DEP forces concentrate at the surface of the polymer. The DEP force is close to zero in the central region and gradually increases towards the edges. By increasing the applied voltage, the DEP forces get higher on the polymer surface, thus increasing the AR of the MLA. The polymer surface in the initial state is almost flat. The DEP force vectors are shown by the white arrows in the insets of Fig. 4(e). As the DEP force is much larger in the edge regions and since the polymer volume is conserved, the edge regions are pulled upward, while the central region is forced down, finally forming a structure with parabolic shape.
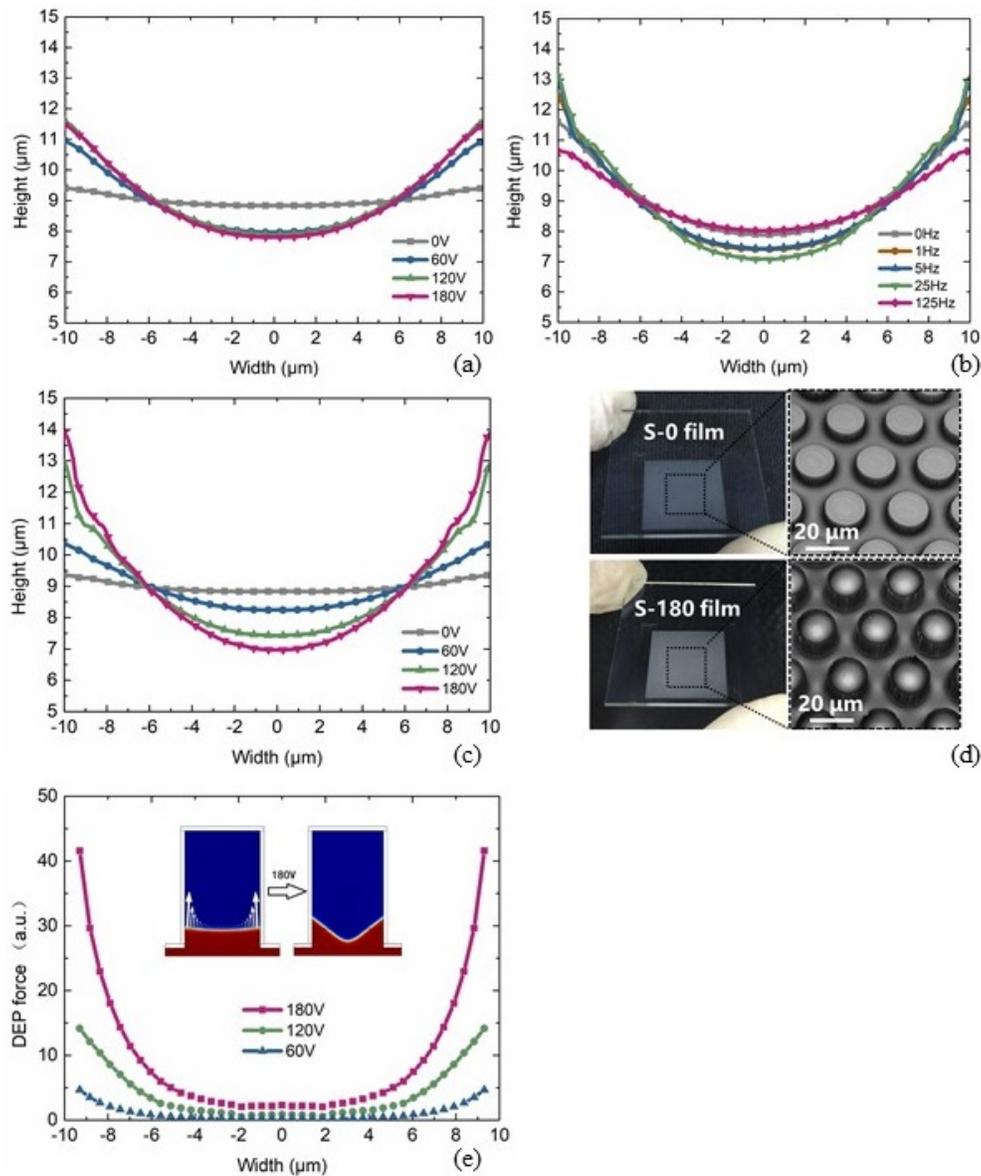
Fig. 4. (a) MLA film surface contour at different constant voltages. (b) MLA surface contour for different square wave frequencies at 120 V (c) MLA surface contour for different square wave voltages at 5 Hz. (d) Photographs (left) and scanning electron microscope images (right, taken under 45° tilt angle) of the S-0 and S-180 films. The size of the patterned area is 20 mm × 20 mm. (e) Simulated DEP force distribution along the meniscus polymer surface for different applied voltages. The insets show the initial state (left) and the final state (right) of the polymer meniscus at 180 V.
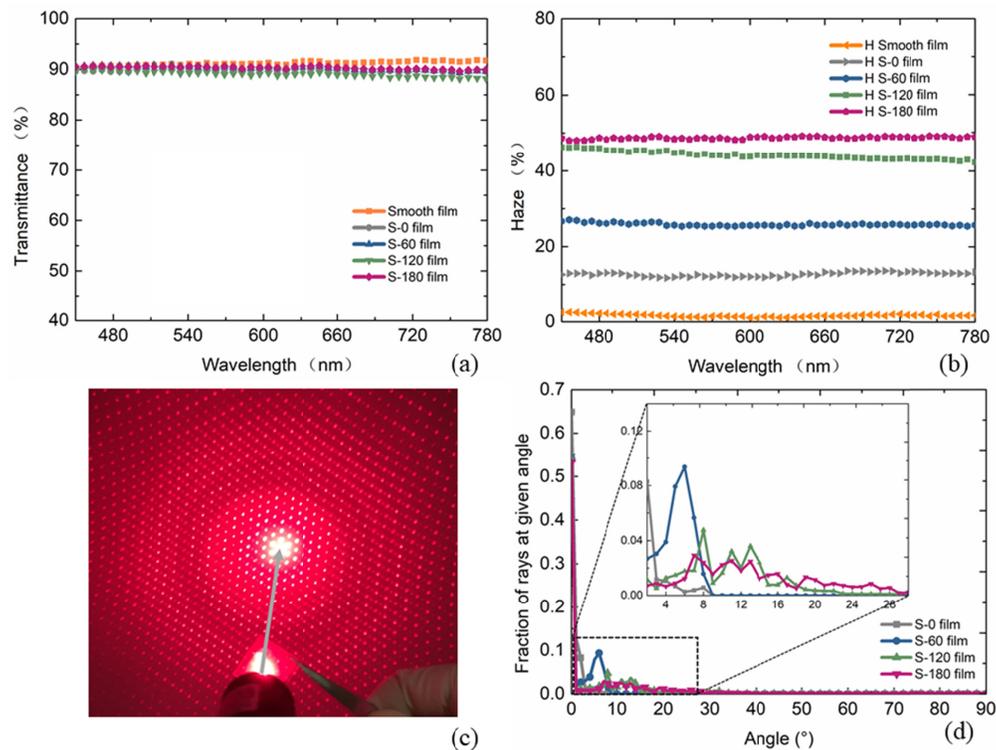
Fig. 5. (a) Overall transmittance and (b) haze (in transmission) spectra of the smooth film plotted together with the spectra of the S-0, S-60, S-120 and S-180 films. (c) Far-field transmission pattern of a 650 nm laser beam irradiating the S-180 film. (d) Simulated angular distribution of the transmitted light rays based on the measured morphologies obtained at different voltages.

Further, we evaluated the optical properties of the resulting light diffusing films. Figure 5(a) shows the measured overall transmittance of MLA films. The transmittance values of the structured film formed at each voltage are slightly lower than for the smooth film, but the average transmittance exceeds 89%. Figure 5(b) shows the measured haze (in transmission) of the MLA films. As the forming voltage increases, the haze values of the films gradually increase from 1.6% (0 V) to 48.7% (180 V). The increase in haze is caused by the refraction of the MLA. When light is incident on the structured surface, it is normally refracted by a large angle according to Snell's law. With higher curvature, the refraction effect is more pronounced, thus enhancing the haze values of the films, namely their diffusion property. Illuminating a laser beam on MLA film samples shows the scattering performance more intuitively, as shown in Fig. 5(c). Under the concave structure, the laser beam is dispersed into a hexagonal array of spots, underlying the good scattering ability of the S-180 film.

To further study the scattering mechanism of light by MLA films, ray optics simulations were performed out of realistic MLA morphologies. As shown in Fig. 5(d), all the samples have a high light intensity peak at 0° because of the relatively large spacing between the microlenses. In the enlarged view, we see that the transmitted light exit angle of S-0 film is less than 9° and distributes mainly in the central region. On the other hand, the light intensity distribution of the DEP force-shaped samples not only concentrates in the central region, but also forms a second peak at a higher angular range. As the applied voltage increases, the peak value of the second peak lowers and the angular spread increases. The maximum exit angle of transmitted light of the S-60 film, S-120 film, and S-180 film is found to be 9°, 25° and 34°,

respectively. This demonstrates that the increase of AR of the MLA surface can more evenly scatter the light into a wider angular range.
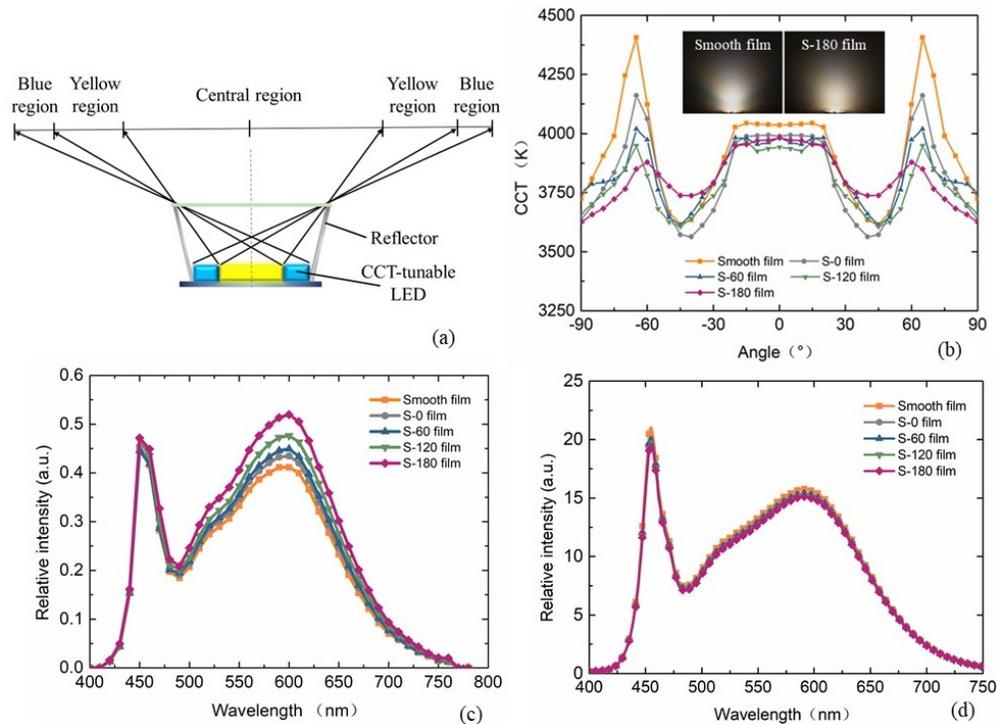
Fig. 6. (a) Schematic of the light distribution in a CCT-tunable LED lamp. (b) Angle-dependent CCT distribution of the lamps covered with the smooth film and with the MLA films. The insets show the photographs of the light spots obtained with a CCT-tunable LED with smooth film (left) and with the S-180V film (right). (c) Emission spectra of different films at the zenith angles of 65°. (d) Emission spectra of the corresponding samples measured with an integrating sphere.

As the fabricated MLA exhibit a high optical transmittance and broaden the angular distribution of transmitted light, they are relevant candidates to improve light management in CCT-tunable LEDs. Figure 6(a) shows a schematic diagram of the light distribution of the CCT tunable LED. The LED is surrounded by a cylindric reflector as desired for practical applications. In the center region above the lamp, the CCT values are uniform because the rays from the warm-white and cold-white areas are not blocked and can be mixed well. In the yellow region the light coming from the cool-white area (located near the reflector), is blocked and cannot transmit to this region. In this part, warm-white light mostly dominates and the CCT is low, resulting in the appearance of a yellow halo. In the blue region, the light from the warm-white area is also shielded, and only the light from cool-white area, which is away from the reflector, illuminates this area. Thus, the CCT of this area is significantly higher than other angles and a blue ring appears.

In view of the light scattering properties of MLA films, we covered the MLA film samples at the top of the CCT-tunable LED lamp for an ACU improvement demonstration. As shown in Fig. 6(b), the CCT curve of the lamp has a large fluctuation when covered with a smooth film. We define the difference between the maximum and minimum CCT values as the CCT deviation, which is as high as 791 K in the smooth film. As the AR of the MLA increases, the CCT deviation of the lamp gradually decreases. Thus, the CCT deviation of the S-180 film configuration is reduced to 357 K. The improvement of the ACU of the lamp is mainly caused by the CCT decrease at a zenith angle of 65°. In other words, it relieves the

blue ring phenomenon. Assisted by the MLA film, the emitting light is refracted and mixed more evenly and more light rays from the warm-white area enter the blue region. Therefore, the CCT at an angle of 65° gradually decreases as the AR of the MLA film increases. The inset shows the light spot patterns of the CCT-tunable LED with the smooth film (left) and the S-180 film (right). It is obvious that the former has a clear blue ring and a yellow halo. The latter has no obvious blue ring and the yellow halo is also significantly reduced.

To verify the analysis regarding the disappearance of the blue ring phenomenon, we extracted and compared the emission spectra for the different configurations considered and for a zenith angle of 65° (see Fig. 6(c)). These spectra display little difference in the peaks of the blue light band (400 nm–500 nm). The enhancement of scattering performance has less effect on the blue light. On the other hand, these measurements indicate significant differences in the yellow portion of the spectra. With increasing applied voltage, the peaks and relative intensity of the yellow light (500 nm–750 nm) spectrum gradually increase. Films with a higher haze (higher AR, see Fig. 5(b)) have a better light diffusing property and more warm-white light can reach the spatial range of 65° which has an overall effect of lowering the resulting CCT at high zenith angles, as observed in Fig. 6(b).

To investigate the influence of the MLA film on the luminous flux, we used an integrating sphere to measure the emission spectrum of the CCT-tunable LED lamp covered with the different films. The driven current is the same as for the ACU measurement and the results are shown in Fig. 6(d). The emission intensity of the CCT-tunable LED lamp upon integration of the MLA films is just slightly lower than by using the smooth film, in accordance with the transmittance values reported in Fig. 5(a). Thus, the maximum luminous flux loss ratio amounts to 4.53% when the lamp is covered with S-180 film and with respect to the smooth film configuration.

In practical applications, CCT-tunable LED lamps need to be adjusted to different CCT ranges according to requirements. To this end, we validated the research results in different CCT ranges. Table 1 lists the CCT deviations and luminous fluxes of CCT-tunable LEDs covered by smooth film and S-180V film over the full CCT range of 2500–6500 K. From the CCT deviation comparison, it is found that as the average CCT value increases, the CCT deviation gradually increases. In each CCT range, the CCT deviation of the S-180V film lamp is significantly reduced compared with the smooth film configuration, which improves the ACU of the LED efficiently. In terms of luminous flux, the lamps covered with S-180V film have slightly narrower CCT range than smooth film, and the decreasing ratio is within 5%. Therefore, the MLA films can effectively improve the ACU of CCT-tunable LEDs and maintain a high luminous flux, which meets the needs of practical applications.

Table 1. Correlated color temperature deviation (ΔCCT) and luminous flux of CCT-tunable LED covered with a smooth film and with the S-180V film for different CCT ranges. The uncertainties of the CCT deviation and luminous flux data were derived out of 3 and 5 measurements, respectively.

CCT Range (K)	ΔCCT (K)		Luminous Flux (lm)	
	Smooth film	S-180V film	Smooth film	S-180V film
2500-3000	454 ± 4	214 ± 4	421.6 ± 0.3	403.9 ± 0.1
3000-4000	772 ± 3	339 ± 2	466.4 ± 0.2	447.2 ± 0.1
4000-5000	791 ± 6	357 ± 3	478.0 ± 0.3	456.4 ± 0.3
5000-6000	997 ± 8	616 ± 7	470.1 ± 0.1	452.7 ± 0.2
6000-6500	1206 ± 14	771 ± 9	472.6 ± 0.2	452.3 ± 0.2

4. Conclusion

In summary, we have presented a novel approach that exploits the electrowetting effect to fabricate MLA with tunable ARs for CCT-tunable LED applications. At the optimized voltage frequency of 5 Hz, the AR of the MLA gradually increases from 0.057 to 0.693 by increasing the applied voltage from 0 V to 180 V, which leads to higher DEP forces. As confirmed experimentally and numerically, the MLA films with higher AR exhibit a higher haze and a broader angular light distribution. When the MLA films are applied to a CCT-tunable LED with a CCT of 3000-4000 K, the CCT deviation is largely reduced and the best ACU performance is achieved with the S-180 MLA film, which has the highest AR of 0.693 among all the fabricated MLA. The S-180 film also shows a remarkable performance for ACU improvement in other CCT ranges and helps to maintain a good lumen output. The ACU enhancement is caused primarily by the homogenous mixing of the warm and of the cool light, caused by the high diffusing property of the MLA film. Our method for the fabrication of MLA with tailorable ARs is facile, rapid and cost-effective. Higher improvements in ACU performances are expected by further optimizing the MLA design, especially by reducing the spacing between the micro-lenses.

References

1. T. F. Zhu, Z. Liu, Z. Liu, F. Li, M. Zhang, W. Wang, F. Wen, J. Wang, R. Bu, J. Zhang, and H. X. Wang, "Fabrication of monolithic diamond photodetector with microlenses," Opt. Express **25**(25), 31586–31594 (2017).
2. J. D. Myers, W. Cao, V. Cassidy, S. H. Eom, R. Zhou, L. Yang, W. You, and J. Xue, "A universal optical approach to enhancing efficiency of organic-based photovoltaic devices," Energy Environ. Sci. **5**(5), 6900–6904 (2012).
3. X. Zhou, Y. Peng, R. Peng, X. Zeng, Y. A. Zhang, and T. Guo, "Fabrication of large-scale micro-lens arrays based on screen printing for integral imaging 3D display," ACS Appl. Mater. Interfaces **8**(36), 24248–24255 (2016).
4. H. Y. Lin, Y. M. Pai, J. X. Shi, X. Y. Chen, C. H. Lin, C. M. Weng, T. Y. Chen, C. C. Lin, M. D. B. Charlton, Y. P. Huang, C. H. Chen, H. P. Chen, and H. C. Kuo, "Optimization of nano-honeycomb structures for flexible w-LEDs," Opt. Express **25**(17), 20466–20476 (2017).
5. X. Luo, R. Hu, S. Liu, and K. Wang, "Heat and fluid flow in high-power LED packaging and applications," Pror. Energy Combust. Sci. **56**, 1–32 (2016).
6. Y. U. Shudong, Y. Tang, L. I. Zongtao, K. Chen, X. Ding, and Y. U. Binhai, "Enhanced optical and thermal performance of white light-emitting diodes with horizontally layered quantum dots phosphor nanocomposites," Photon. Res. **6**(2), 90 (2018).
7. S. Yu, Y. Tang, Z. Li, Y. Chen, B. Yu, and G. Liang, "Freeform illumination lens design combining energy and intensity mapping," Opt. Eng. **56**(4), 045101 (2017).
8. X. Ding, M. Li, Z. Li, Y. Tang, Y. Xie, X. Tang, T. Fu," Thermal and optical investigations of a laser-driven phosphor converter coated on a heat pipe," App. Thermal Engin. **148**, 1099-1106 (2019).
9. Y. Peng, Y. Mou, Y. Zhuo, H. Li, X. Z. Wang, M. X. Chen, and X. B. Luo, "Preparation and luminescent performances of thermally stable redemitting phosphor-in-glass for high-power lighting," J. Alloys Compd. **768**, 114–121 (2018).
10. J. S. Li, Y. Tang, Z. T. Li, X. R. Ding, L. S. Rao, and B. H. Yu, "Effect of Quantum Dot Scattering and Absorption on the Optical Performance of White Light-Emitting Diodes," IEEE Trans. Electron. Dev. **65**, 2877–2884 (2018).

11. Z. Huai, L. Sheng, and L. Xiaobing, "Enhancing Angular Color Uniformity of Phosphor-Converted White Light-Emitting Diodes by Phosphor Dip-Transfer Coating," J. Lightwave Technol. **31**(12), 1987–1993 (2013).

12. S. Yu, B. Zhuang, J. Chen, Z. Li, L. Rao, B. Yu, and Y. Tang, "Butterfly-inspired micro-concavity array film for color conversion efficiency improvement of quantum-dot-based light-emitting diodes," Opt. Lett. **42**(23), 4962–4965 (2017).

13. L. Rao, Y. Tang, Z. Li, X. Ding, J. Li, S. Yu, C. Yan, and H. Lu, "Effect of ZnO nanostructures on the optical properties of white light-emitting diodes," Opt. Express **25**(8), A432–A443 (2017).

14. Y. Tang, Z. Li, Z.-T. Li, J.-S. Li, S.-D. Yu, and L.-S. Rao, "Enhancement of Luminous Efficiency and Uniformity of CCT for Quantum Dot-Converted LEDs by Incorporating With ZnO Nanoparticles," IEEE Trans. Electron Dev. **65**(1), 158–164 (2018).

15. J.-S. Li, Y.-H. Chen, Z.-T. Li, S.-D. Yu, Y. Tang, X.-R. Ding, and W. Yuan, "ACU Optimization of pc LEDs by Combining the Pulsed Spray and Feedback Method," J. Disp. Technol. **12**(10), 1229–1234 (2016).

16. J.-S. Li, C.-M. Yan, Z.-T. Li, G.-W. Liang, Y. Tang, and B.-H. Yu, "Color Uniformity Enhancement for WLEDs Using Inverted Dispensing Method," IEEE Photonics Technol. Lett. **29**(23), 2079–2082 (2017).

17. Y. Tang, G. Liang, J. Chen, S. Yu, Z. Li, L. Rao, and B. Yu, "Highly reflective nanofiber films based on electrospinning and their application on color uniformity and luminous efficacy improvement of white light-emitting diodes," Opt. Express **25**(17), 20598–20611 (2017).

18. H. C. Kuo, C. W. Hung, H. C. Chen, K. J. Chen, C. H. Wang, C. W. Sher, C. C. Yeh, C. C. Lin, C. H. Chen, and Y. J. Cheng, "Patterned structure of remote phosphor for phosphor-converted white LEDs," Opt. Express **19**(S4 Suppl 4), A930–A936 (2011).

19. S. Yu, Z. Li, G. Liang, Y. Tang, B. Yu, and K. Chen, "Angular color uniformity enhancement of white light-emitting diodes by remote micro-patterned phosphor film," Photon. Res. **4**(4), 140 (2016).

20. Q. Chen, Z. Li, K. Chen, Y. Tang, X. Ding, and B. Yu, "CCT-tunable LED device with excellent ACU by using micro-structure array film," Opt. Express **24**(15), 16695–16704 (2016).

21. A. Lee, H. Chen, S. C. Tan, and S. Y. R. Hui, "Precise Dimming and Color Control of Light-Emitting Diode Systems based on Color Mixing," IEEE Trans. Power Electron. **2015**, 1 (2015).

22. A. T. L. Lee, J. K. O. Sin, and P. C. H. Chan, "Scalability of Quasi-Hysteretic FSM-Based Digitally Controlled Single-Inductor Dual-String Buck LED Driver to Multiple Strings," IEEE Trans. Power Electron. **29**(1), 501–513 (2014).

23. C. Y. Liu, K. J. Chen, D. W. Lin, C. Y. Lee, C. C. Lin, S. H. Chien, M. H. Shih, G. C. Chi, C. Y. Chang, and H. C. Kuo, "Improvement of emission uniformity by using micro-cone patterned PDMS film," Opt. Express **22**(4), 4516–4522 (2014).

24. J. Yong, F. Chen, Q. Yang, G. Du, H. Bian, D. Zhang, J. Si, F. Yun, and X. Hou, "Rapid fabrication of large-area concave microlens arrays on PDMS by a femtosecond laser," ACS Appl. Mater. Interfaces **5**(19), 9382–9385 (2013).

25. R. Ahmed, A. K. Yetisen, and H. Butt, "High Numerical Aperture Hexagonal Stacked Ring-Based Bidirectional Flexible Polymer Microlens Array," ACS Nano **11**(3), 3155–3165 (2017).

26. J. Tan, M. Shan, C. Zhao, and J. Liu, "Design and fabrication of diffractive microlens arrays with continuous relief for parallel laser direct writing," Appl. Opt. **48**, 340–345 (2008).

27. M. Severi and P. L. Mottier, "Etching selectivity control during resist pattern transfer into silica for the fabrication of microlenses with reduced spherical aberrations," Opt. Eng. **38**(1), 146–150 (1999).

28. A. M. B. Stern and T. R. Jay, "Dry etching for coherent refractive microlens arrays," Opt. Eng. **33**(11), 3547–3551 (1994).

29. Z. D. Popovic, R. A. Sprague, and G. A. Connell, "Technique for monolithic fabrication of microlens arrays," Appl. Opt. **27**(7), 1281–1284 (1988).

30. J. Zhang, C. Wang, J. Zeng, and A. J. Pang, "A Low Cost Bumping Method for Flip Chip Assembly and MEMS Integration," IEEE Trans. Compon. Packag. Tech. **30**(4), 781–786 (2007).

31. H. Jung and K. H. Jeong, "Monolithic polymer microlens arrays with high numerical aperture and high packing density," ACS Appl. Mater. Interfaces **7**(4), 2160–2165 (2015).

32. C. Y. Chang, S. Y. Yang, L. S. Huang, and J. H. Chang, "Fabrication of plastic microlens array using gas-assisted micro-hot-embossing with a silicon mold," Infrared Phys. Technol. **48**(2), 163–173 (2006).

33. D. Xie, X. Chang, X. Shu, Y. Wang, H. Ding, and Y. Liu, "Rapid fabrication of thermoplastic polymer refractive microlens array using contactless hot embossing technology," Opt. Express **23**(4), 5154–5166 (2015).

34. X. J. Shen and L. Lin, Micro Plastic Embossing Process: Experimental and Theoretical Characterizations (Springer Berlin Heidelberg, 2001).

35. M. Kuang, L. Wang, and Y. Song, "Controllable printing droplets for high-resolution patterns," Adv. Mater. **26**(40), 6950–6958 (2014).

36. J. Y. Kim, N. B. Brauer, V. Fakhfouri, D. L. Boiko, E. Charbon, G. Grutzner, and J. Brugger, "Hybrid polymer microlens arrays with high numerical apertures fabricated using simple ink-jet printing technique," Opt. Mater. Express **1**(2), 259–269 (2011).

37. R. Hünig, A. Mertens, M. Stephan, A. Schulz, B. Richter, M. Hetterich, M. Powalla, U. Lemmer, A. Colsmann, and G. Gomard, "Flower Power: Exploiting Plants' Epidermal Structures for Enhanced Light Harvesting in Thin Film Solar Cells," Adv. Opt. Mater. **4**(10), 1487–1493 (2016).

38. B. Fritz, R. Hünig, R. Schmager, M. Hetterich, U. Lemmer, and G. Gomard, "Assessing the influence of structural disorder on the plant epidermal cells' optical properties: a numerical analysis," Bioinspir. Biomim. **12**(3), 036011 (2017).

39. Y. Peng, Y. Mou, X. Guo, X. Xu, H. Li, M. Chen, and X. Luo, "Flexible fabrication of a patterned red phosphor layer on a YAG:Ce3+ phosphor-in-glass for high-power WLEDs," Opt. Mater. Express **8**(3), 605 (2018).

40. Q. Xu, B. Dai, Y. Huang, H. Wang, Z. Yang, K. Wang, S. Zhuang, and D. Zhang, "Fabrication of polymer microlens array with controllable focal length by modifying surface wettability," Opt. Express **26**(4), 4172–4182 (2018).

41. C. Fang, J. Zheng, Y. Zhang, Y. Li, S. Liu, W. Wang, T. Jiang, X. Zhao, and Z. Li, "Antireflective Paraboloidal Microlens Film for Boosting Power Conversion Efficiency of Solar Cells," ACS Appl. Mater. Interfaces **10**(26), 21950–21956 (2018).

42. Y. Peng, X. Guo, R. Liang, Y. Mou, H. Cheng, M. Chen, and S. Liu, "Fabrication of Microlens Arrays with Controlled Curvature by Micromolding Water Condensing Based Porous Films for Deep Ultraviolet LEDs," ACS Photonics **4**(10), 2479–2485 (2017).

43. B. Yang, J. Zhou, Q. Chen, L. Lei, and K. Wen, "Fabrication of hexagonal compound eye microlens array using DMD-based lithography with dose modulation," Opt. Express **26**(22), 28927–28937 (2018).

44. X. Li, Y. Ding, J. Shao, H. Liu, and H. Tian, "Fabrication of concave microlens arrays using controllable dielectrophoretic force in template holes," Opt. Lett. **36**(20), 4083–4085 (2011).

45. X. Li, Y. Ding, J. Shao, H. Tian, and H. Liu, "Fabrication of microlens arrays with well-controlled curvature by liquid trapping and electrohydrodynamic deformation in microholes," Adv Mater 24, OP165–169, OP190 (2012).

46. M. Vallet, B. Berge, and L. Vovelle, "Electrowetting of water and aqueous solutions on poly(ethylene terephthalate) insulating films," Polymer (Guildf.) **37**(12), 2465–2470 (1996).

47. X. Li, J. Shao, H. Tian, Y. Ding, and X. Li, "Fabrication of high-aspect-ratio microstructures using dielectrophoresis-electrocapillary force-driven UV-imprinting," J. Micromech. Microeng. **21**(6), 065010 (2011).

48. X. Li, H. Tian, J. Shao, Y. Ding, and H. Liu, "Electrically modulated microtransfer molding for fabrication of micropillar arrays with spatially varying heights," Langmuir **29**(5), 1351–1355 (2013).

49. X. Li, H. Tian, Y. Ding, J. Shao, and Y. Wei, "Electrically templated dewetting of a UV-curable prepolymer film for the fabrication of a concave microlens array with well-defined curvature," ACS Appl. Mater. Interfaces **5**(20), 9975–9982 (2013).

50. H. Tian, J. Shao, Y. Ding, X. Li, and X. Li, "Numerical studies of electrically induced pattern formation by coupling liquid dielectrophoresis and two-phase flow," Electrophoresis **32**(17), 2245–2252 (2011).

51. D. Jacqmin, Calculation of Two-Phase Navier–Stokes Flows Using Phase-Field Modeling (Academic Press Professional, Inc., 1999).

52. C. Zhou, P. Yue, J. J. Feng, C. F. Ollivier-Gooch, and H. H. Hu, "3D Phase-Field Simulations of Interfacial Dynamics in Viscoelastic Fluids with Adaptive Meshing," in 61st Annual Meeting of the APS Division of Fluid Dynamics (2008).

53. X. Li, H. Tian, J. Shao, Y. Ding, X. Chen, L. Wang, and B. Lu, "Decreasing the Saturated Contact Angle in Electrowetting-on-Dielectrics by Controlling the Charge Trapping at Liquid-Solid Interfaces," Adv. Funct. Mater. **26**(18), 2994–3002 (2016).